Highly Thermal Stable Broadband Near-Infrared Luminescence in Ni^{2+}-doped $LaAlO_3$ with Charge Compensator

Jumpei Ueda[1,2], Tomoaki Minowa[1], Jian Xu[1,3], Shogo Tanaka[1], Takayuki Nakanishi[4], Takashi Takeda[4], Setsuhisa Tanabe[1]*

[1] Graduate School of Human and Environmental Studies, Kyoto University, Yoshida-Nihonmatsu-cho, Sakyo-ku, Kyoto 606-8501, Japan

[2] Graduate School of Advanced Science and Technology, Japan Advanced Science and Technology (JAIST), 1-1 Asahidai, Nomi, Ishikawa 923-1292, Japan

[3] International Center for Young Scientists (ICYS), National Institute for Materials Science (NIMS), Tsukuba, 305-0044, Japan

[4] Luminescent Materials Group, National Institute for Materials Science (NIMS), Tsukuba, 305-0044, Japan

Keywords: NIR, Phosphor, Ni^{2+}, Perovskite, Quenching

ABSTRACT

Ni^{2+}-doped $LaAlO_3$ perovskite ceramic samples with a charge compensator (M^{4+}) were prepared and their luminescent properties were investigated. The $LaAlO_3:Ni^{2+}$-M^{4+} (M = Sn, Hf, Ti, Zr) perovskites show a broad near-infrared (NIR) luminescence peaking at around 1070 nm with 150 nm FWHM due to the Ni^{2+}:$^3T_2$-$^3A_2$ transition. The Sn^{4+}-codoped one showed the highest NIR luminescence intensity. The valence state of major Ni ions is changed from Ni^{3+} to Ni^{2+} by co-doping with Sn^{4+} based on X-ray absorption spectroscopy. The $LaAlO_3:Ni^{2+}$-Sn^{4+} shows the shortest luminescence peak wavelength (λ_{em} = 1070nm) at 300 K due to the strong crystal field and also shows the highest quenching temperature, $T_{50\%}$ of 608 K in the temperature dependence of PL intensity, due to the largest activation energy among the Ni^{2+}-doped NIR phosphors ever reported. Based on the positive trend in the plot of $T_{50\%}$ vs PL peak energy, it is concluded that the dominant quenching process in almost all Ni^{2+} phosphors is the thermally activated crossover process. It is also demonstrated that the luminescence peak wavelength is shifted from 1070 nm to 1235 nm continuously by substituting Ga ions for the Al site.

Introduction

Near-infrared (NIR) spectroscopy is one of the important technologies for sensing and tracing chemical substances in non-destructive and non-contact manners, leading to significant applications such as pharmaceutical technology, medical diagnosis, food quality assessment, agriculture analysis, bio imaging and so on[1-6]. NIR phosphor-converting light emitting diode (pc-LEDs) have attracted much attention as a broad NIR light source instead of old fashioned tungsten lamps because of the high electric-light conversion efficiency, long lifetime, stable intensity, low cost and small device size[7-10]. In general, the NIR region is from 700 nm to 2500 nm; if a NIR pc-LED covers the whole NIR range, it becomes a comparable light source to the tungsten lamp. On the other hand, the NIR pc-LED with a selective wide wavelength range is also practically useful based on the biological windows of NIR-I, II, III (I: 650 ~ 950 nm, II: 1000 ~ 1350 nm, III: 1300 ~ 1700 nm) [11, 12] and the sensitivity curves of Si photodiodes and CCDs (190 ~ 1100 nm) and InGaAs photodiodes and camera (high sensitivity type: 900 ~ 1700 nm, long wavelength type: 900 ~ 2600 nm).

For the NIR pc-LED in the NIR-I wavelength region, many Cr^{3+}-doped NIR phosphors utilizing the $^4T_2 \rightarrow {}^4A_2$ transition have been studied and commercialized successfully[10]. Although the luminescence wavelength of the Cr^{3+}: $^4T_2 \rightarrow {}^4A_2$ transition can be controlled by the crystal field splitting, almost all Cr^{3+}-doped NIR phosphors show shorter peak wavelength than 1000 nm[13]. On the other hand, the Cr^{4+} ion in the tetrahedral site with the $^3T_2$-$^3A_2$ transition, which is also sensitive to the crystal field, is one of the suitable candidate phosphors for luminescence above 1000 nm luminescence. The luminescence peak wavelength of Cr^{4+}-doped phosphors has been reported in the range between 1150 nm and 1600 nm[13, 14]. Therefore, it is not easy to cover the luminescence wavelength from 1000 nm to 1150 nm only by the Cr^{3+} and Cr^{4+}-based NIR

phosphors. In order to realize the luminescence in this region, a quite weak and strong crystal fields are necessary for the Cr^{3+} ion in the octahedral site and the Cr^{4+} ion in the tetrahedral site, respectively.

In this study, we focus on the Ni^{2+} ion in the octahedral site. The Ni^{2+} ion has $[Ar]3d^8$ electronic configuration and the energy levels follow the d^8 Tanabe-Sugano diagram[15, 16], which is the same energetic structure as Cr^{4+} ($[Ar]3d^2$) in the tetrahedral site (Figure **1**). Until now, Ni^{2+}-doped NIR phosphors with $^3T_2 \rightarrow {}^3A_2$ broad NIR luminescence have also been studied well for applications of NIR solid-state lasers and NIR LEDs in many host materials such as MgO[17, 18], $LiGa_5O_8$[19], $LaMgAl_{11}O_{19}$[20], Garnets[21-24], perovskites[25-31], spinel[32-35], $Zn(Al,Ga)O_4$ [36-38] and so on [39, 40]. The $^3T_2$ energy level is very sensitive to the crystal field as shown in Figure **1**. Therefore, the Ni^{2+}: $^3T_2$-$^3A_2$ luminescence wavelength can be controlled by tuning the crystal field. The peak wavelength of the reported Ni^{2+}-doped phosphors listed above are located between 1100 nm and 2000 nm. In order to shift the $^3T_2$ energy level to the higher energy (1000 nm to 1100 nm in wavelength), the AlO_6 octahedral site with a relatively small size is focused because of the possibility of the high crystal field. Here, we selected the lanthanum aluminate perovskite ($LaAlO_3$) host material. The general oxide perovskites are expressed by ABO_3, in which *A*-site has the12-fold coordination and B-site is the octahedral site. Since the luminescence peak of $YAlO_3:Ni^{2+}$ was reported to be 1100 nm[21], it is expected that the $LaAlO_3$ also becomes a suitable host with a strong crystal field. However, the detailed spectroscopy of $LaAlO_3:Ni^{2+}$ has never been reported. Also, the Ni^{2+} ion stabilization in the $LaAlO_3$ host is needed to be discussed because the Ni ion can take both 2+ and 3+ valence states. The Ni ion in the pure $LaAlO_3$ host may prefer the Ni^{3+} state owing to the trivalent Al site. Actuality, the $LaNiO_3$ perovskite with Ni^{3+} is known to exist.[41, 42] In order to stabilize the Ni^{2+} ion in the $LaAlO_3$, a charge

compensator must be adopted; the Ni'_{Al} state should be compensated by any of $M_{La}^{\cdot}$, $M_{Al}^{\cdot}$ and $V_O^{\cdot}$ defects (M is a tetravalent metal ion). Considering candidates of M^{4+} ions with proper ionic radius and the controllability of the defect concentration, a suitable M^{4+} ion in the Al site should be explored as a charge compensator. Here, several charge compensators are tested and the Ni valence states were investigated by XANES (X-ray Absorption Near Edge Structure) spectroscopy. The luminescence properties and its temperature dependence of $LaAlO_3:Ni^{2+}$ with a proper charge compensator are investigated in detail. Also, the tunability of luminescence wavelength is examined by changing Ga^{3+} substitution for the B-site Al^{3+} ion in $LaAlO_3$.

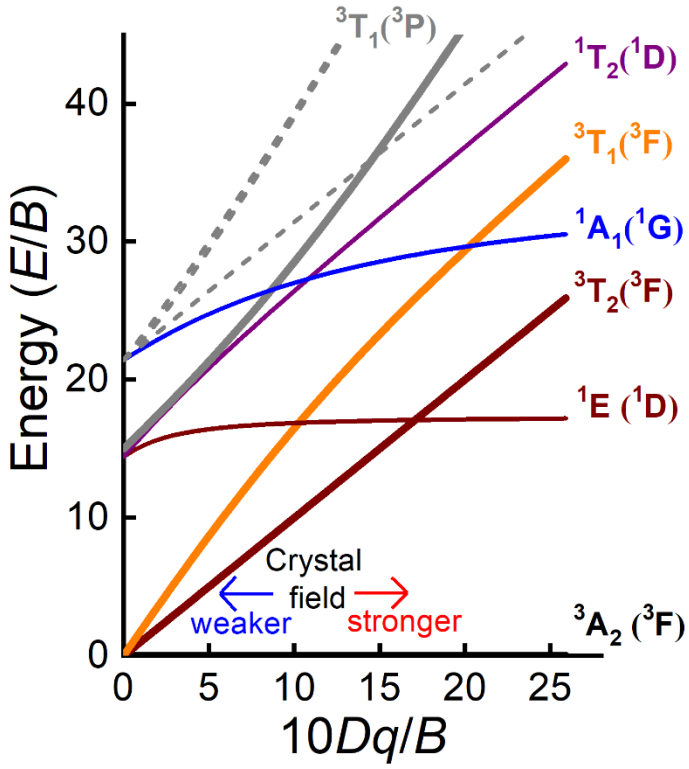

Figure 1. General Tanabe-Sugano diagram for the d^8 electron configuration in the octahedral crystal field, C/B=4.71 and B=1030 cm^{-1}.

Experimental Section

Material preparation

Ceramic samples with $LaAl_{0.995}Ni_{0.005}O_3$, $LaAl_{0.99}Ni_{0.005}M_{0.005}O_3$ (M = Hf, Sn, Ti, Zr), $LaAl_{0.995}Ni_{0.005}Sn_{0.01}O_3$ and $La(Al_{1-x}Ga_x)_{0.99}Ni_{0.005}Sn_{0.005}O_3$ (x=0, 0.25, 0.5, 0.75, 1) compositions were prepared by solid-state reaction. Here, the lanthanum aluminate perovskite (LAP) samples are referred as LAP:Ni and LAP:Ni-M (M = Hf, Mn, Sn, Ti, Zr). La_2O_3 (99.99%, Furuuchi Chemical), Al_2O_3 (99.99%, Taimei Chemicals), NiO (99.99%, Sigma-ALDRICH), HfO_2 (99.98%, Kojundo KOJUNDO CHEMICAL LABORATORY), SnO_2 (99.99%, KOJUNDO CHEMICAL LABORATORY), TiO_2 (99.99%, Mitsuwa Chemicals), ZrO_2 (99.99%, Furuuchi Chemical) were used as starting chemicals. In order to remove moisture, the hygroscopic La_2O_3 chemical was heat-treated at 800℃ for 10 h and then kept in a glove box filled with Ar gas. The chemicals were mixed with alumina balls (ϕ 1mm, SSA-999W, Nikkato) and 20 mL ethanol in an alumina jar by a ball mill (Premium Line P-7, Fritsch) with the condition (400 rpm, 30 min × 2 times). Drying the obtained slurry, the powder was heated at 1000 °C for 10 h. Pellets with 13 mm diameter were made and then sintered at 1500 ℃ for 10 h.

Crystal structure and valence state

The crystal structure of the obtained samples was investigated by an X-ray diffraction (XRD) apparatus (XRD-6000, Shimadzu). The XRD patterns were compared with reference XRD patterns which were simulated from the crystal structure data in ICSD (Inorganic Crystal

Structure Database). The valence state of Ni ion in the $LaAlO_3$ host was checked by XANES (X-ray Absorption Near Edge Structure) spectroscopy in the beamline BL-9A of Photon Factory (KEK, Japan). The obtained XANES spectra were analyzed using Athena software package[43].

Optical Measurements

The PL spectra in the NIR region were measured using a multi-channel NIR spectrometer (NIRQUEST, Ocean Optics) by 600 nm excitation light, which is generated by a Xe lamp (MAX302, Asahi Spectra) and two filters of a 600 nm band-pass filter with 40 nm FWHM (FBH600-40, Thorlabs) and an additional 900 nm short-pass filter (FESH900, Thorlabs) to exclude stray light in the NIR region. The PL spectra were calibrated by a standard halogen lamp (DH-2000-RECAL-EXT, Ocean Optics) into the photon flux spectrum. The PLE spectra were measured using a self-build setup; the monochromatic light is generated by two monochromators (SpectraPro-300i, Acton) and a halogen lamp (TS-428, Acton) in the range 500 and 1050nm and a Xe lamp (PE300BUV, Excelitas Cermax) in the range 250 nm and 500 nm. The luminescence was detected by an InGaAs photodiode with a 1050 nm long-pass filter (FELH1050, Thorlabs). The PLE spectra were calibrated by photon flux spectrum of excitation light which is measured using a standard Si photodiode (S1337-1010BQ, Bunkoukeiki). In order to control the temperature, a cryostat (CRT-A020-SE00, Ulvac Cryogenics) with vacuum in the range from 3.5K to 300K and a thermal stage (10035L, Japan High Tech) with N_2 atmosphere in the range from 80 K to 800 K were used. The energy level calculation was executed using the same calculation method in the previous paper[44].

The luminescence decay curves were measured by a fluorescence lifetime spectrometer (Quantaurus-Tau C11367-02, Hamamatsu Photonics). An optional Xe flash lamp with a 600 nm band-pass filter (FBH600-40, Thorlabs, Inc), a 550 nm colored glass filter and a 950 nm short-pass filter (FESH950, Thorlabs, Inc) was used as an excitation source. The luminescence wavelength was selected by a 900 nm long-pass filter and a built-in grating. In order to control the temperature, a cryostat (CRT-006-2000, Iwatani) in the range 20K and 300K and another cryostat (LT3 Helitran, Advanced Research System) in the range 80 K and 800 K were used.

Internal quantum efficiency was measured by a NIR fluorescence spectrophotometer (FP-8750, JASCO Corporation) with a calibrated integrating sphere.

Results and Discussion

Crystal structure

Figure 2 shows XRD patterns of the prepared LAP samples doped with Ni^{2+} and various co-dopants with the reference data of the $LaAlO_3$ (ICSD: 191409). The XRD peaks of all the prepared LAP samples correspond to that of reference $LaAlO_3$ perovskite ($R\bar{3}c$). There are not any other XRD peaks due to impurity phases in the LAP:0.5%Ni^{2+}-0.5%M^{4+}(M=Sn, Ti, Hf). For the LAP:0.5%Ni^{2+}-0.5%Zr^{4+} and LAP:0.5%Ni^{2+}-1%Sn^{4+}, weak unknown XRD peaks at around 28° and 30° were observed. However, it does not affect the main spectroscopic discussion part because the LAP:0.5%Ni^{2+}-0.5%Sn^{4+} without any impurity phases were used for the spectroscopic investigation.

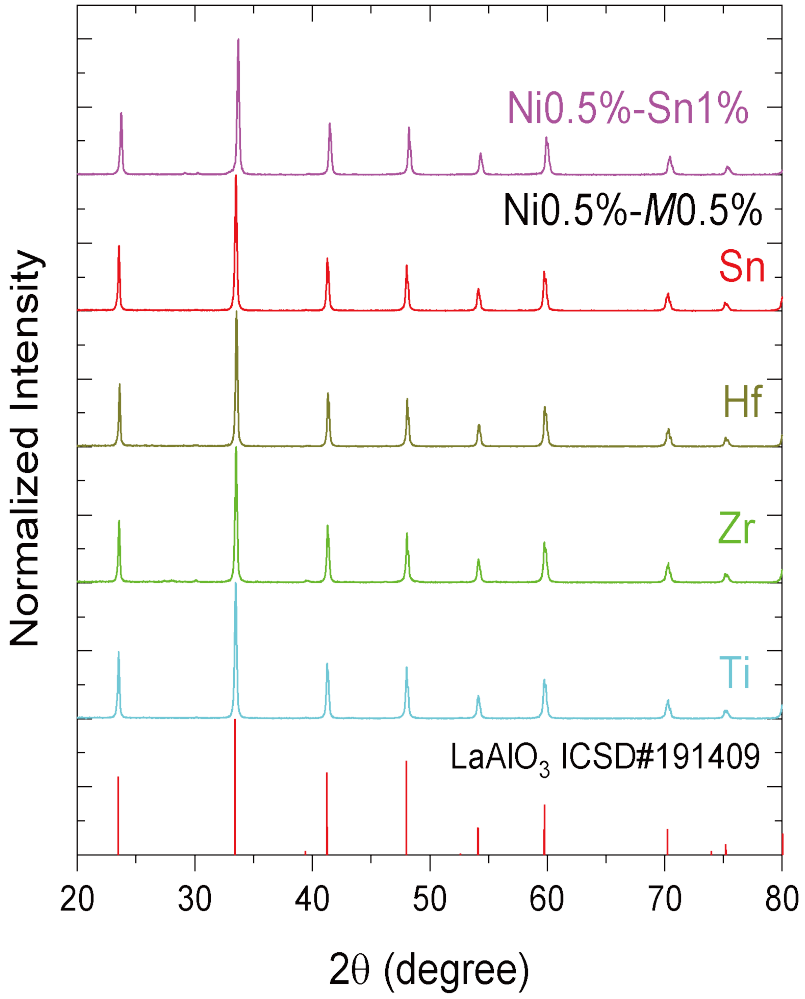

Figure 2. XRD pattern of the LAP:Ni(0.5%)-*M*(0.5%) (M=Ti, Zr, Hf, Sn) and LAP:Ni(0.5%)-Sn(1%) with the reference data of the $LaAlO_3$ (ICSD #191409).

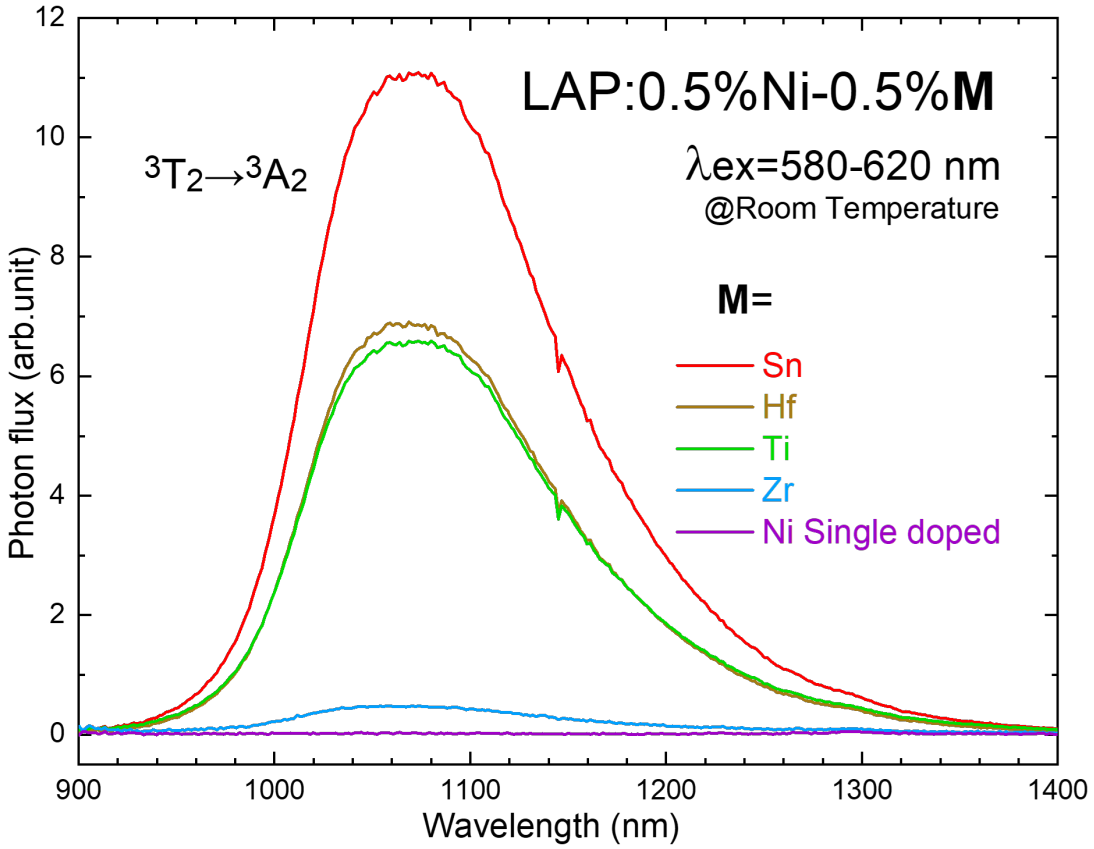

Figure 3. PL spectra of the LAP:0.5%Ni and LAP:0.5%Ni-0.5%M (M =Sn, Hf, Ti, Zr) samples by 600 nm excitation at room temperature.

Effect of charge compensator

Figure 3 shows PL spectra in the NIR region of LAP:0.5%Ni and LAP:0.5%Ni-0.5%M (M =Sn, Hf, Ti, Zr) samples at room temperature. All the LAP:0.5%Ni-0.5%M (M =Sn, Hf, Ti, Zr) samples show strong luminescence peaking at around 1070 nm (Note that a small dip at 1145 nm is due to the error by a pixel of the NIR spectrometer.). The similar broad NIR luminescence around 1100 nm due to the $^3T_{2g} \rightarrow {}^3A_{2g}$ transition of Ni^{2+} was reported in $YAlO_3$ perovskite doped with Ni^{2+} ion.[21] Thus, the observed NIR luminescence can be attributed to the Ni^{2+}: $^3T_{2g}$

$\rightarrow {}^3A_{2g}$ transition. The small blue shift for the Ni^{2+} NIR luminescence band in the $LaAlO_3$ host can be caused by the different crystal fields between $YAlO_3$ and $LaAlO_3$ perovskites.

Compared with Ni singly doped sample, all the samples with tetravalent co-dopants show stronger PL intensity. The tetravalent metal ions (M^{4+}) in Al^{3+} site can act as a charge compensator for the Ni^{2+} ion in the Al^{3+} site. The enhancement of the NIR luminescence intensity of co-doped samples can be caused by the stabilization of Ni^{2+} in the $LaAlO_3$ perovskites. When the type of tetravalent metal ions is changed, the NIR luminescence becomes stronger in the order of Zr, Ti, Hf and Sn co-doped samples. In the series of $LaAlO_3$:Ni-*M* samples, the Sn^{4+} is found to be the best co-dopant to enhance the Ni^{2+} NIR luminescence intensity. The ionic radii of Zr^{4+}, Hf^{4+}, Sn^{4+} and Ti^{4+} in the 6-fold coordination are 0.72, 0.71, 0.69 and 0.605 Å, which are larger by 35%, 33%, 29% and 13% than Al^{3+} (0.535Å). The PL intensity increases in the order of the Zr^{4+}, Hf^{4+} and Sn^{4+} co-doped samples except the Ti^{4+} co-doped one, which indicates that the solubility of co-dopant ions into $LaAlO_3$ can be related to the stabilization of Ni^{2+}. For instance, the Zr^{4+} co-doped sample shows the small XRD peaks of an impurity phase, which implies the low solubility of Zr^{4+} and the weak effect for Ni^{2+} stabilization. On the other hand, it is still unknown why the PL intensity of the Ti^{4+} co-doped sample is weaker than that of the Sn^{4+} co-doped sample. There may be additional effect except the solubility. We also investigated the effect of the atmosphere for the sintering and post-annealing process. However, the sintering of LAP:Ni^{2+} under 95%N_2-5%H_2 and the post-annealing of LAP:0.5%Ni^{2+}-0.5%Sn^{4+} under the different atmospheres (air, N_2, 95%N_2-5%H_2) do not affect to the NIR luminescence intensity (See Fig. S1 in Supporting Information.).

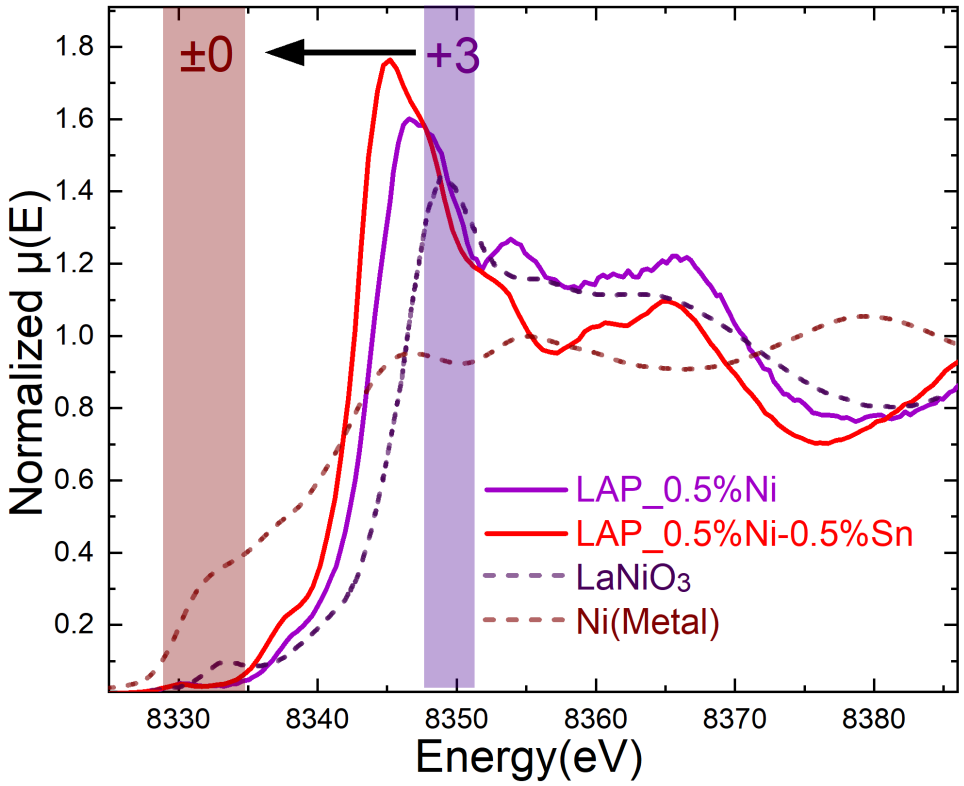

Figure 4. XANES spectra near the Ni K-edge of the LAP:0.5%Ni samples with/without 0.5%Sn and the $LaNiO_3$ and Ni metal references.

In order to check the effect of the charge compensator for the Ni valence state, the Ni K-edge XANES spectra of the LAP:0.5%Ni and LAP:0.5%Ni-0.5%Sn samples were measured (Figure 4). As references, the XANES spectra of Ni metal and $LaNiO_3$ were also investigated. The XANES edge of Ni can be shifted by not only the valence state but also the type of compounds. Because there is no good reference of Ni^{2+} in the perovskite structure, the Ni metal was selected as a reference for the low valence state of Ni. The Ni K-edge absorption peak in the perovskite samples is shifted to lower energy in the order of $LaNiO_3$, LAP:0.5%Ni and LAP:0.5%Ni-

0.5%Sn. Because the Ni valence state is trivalent in the $LaNiO_3$ perovskite, the XANES peak at 8349 eV is characteristic of Ni^{3+} in oxide perovskites. On the other hand, the XANES peak of Ni metal is located at the lowest energy. These results follow a general trend that the XANES peak shifts to lower energy with decreasing valence state. Therefore, LAP:0.5%Ni-0.5%Sn LAP are expected to take the lower valence state of Ni^{2+}. This valence state was also confirmed by the observed NIR luminescence. Also, the XANES peak at 8345 eV of LAP: 0.5%Ni-0.5%Sn with the charge compensator is different from that at 8346 eV of LAP:Ni. These results indicate that LAP:Ni includes both Ni^{2+} and Ni^{3+} and LAP:0.5%Ni-0.5%Sn dominantly has Ni^{2+}. In the $LaAlO_3$ doped with NiO, which is the starting chemical, if Ni^{2+} is not oxidized and the charge neutrality is kept by the oxide vacancy, the defect reaction can be expressed by following equation.

$$La_2O_3 + 2NiO \xrightarrow{LaAlO_3} 2La_{La}^{\times} + 2Ni_{Al}^{'} + 5O_O^{\times} + V_{\ddot{O}}$$

However, Ni^{2+} can be oxidized as following defect reaction because the sample was sintered under air.

$$La_2O_3 + 2NiO + \frac{1}{2}O_2 \xrightarrow{LaAlO_3} 2La_{La}^{\times} + 2Ni_{Al}^{\times} + 6O_O^{\times}$$

Based on the above both defect reactions, the LAP:Ni sample results in the mixed valence states of Ni^{2+} and Ni^{3+}. On the other hand, by co-doping Sn^{4+}, the Ni^{2+} ion was stabilized according to the following defect reaction.

$$La_2O_3 + NiO + SnO_2 \xrightarrow{LaAlO_3} 2La_{La}^{\times} + Ni_{Al}^{'} + Sn_{Al} + 6O_O^{\times}$$

Based on the XANES and NIR PL results, it is clarified that the Sn^{4+} ion act as a charge compensator for the Ni^{2+} ion in the $LaAlO_3$ host.

Determination of Ni^{2+} energy levels based on low temperature spectroscopy

In order to determine the detailed energy levels of Ni^{2+} in the $LaAlO_3$ perovskite, PL and PLE spectra were measured at 3.6 K of the LAP:0.5%Ni-0.5%Sn sample that showed the strongest luminescence intensity (Figure 5). The $LaAlO_3$ crystal structure belongs to $R\bar{3}c$ space group and the Al site has S_6 symmetry. Because the Ni^{2+} ion occupies the Al octahedral site, each energy level in the ideal octahedral site with O_h symmetry can be split into multiple levels. However, we first discuss the energy levels assuming the ideal O_h symmetry to compare the Tanabe-Sugano diagram. In the PL spectrum excited by 600 nm, several sharp PL lines due to the $^3T_{2g} \rightarrow {}^3A_{2g}$ were observed in the range from 1000 nm and 1200 nm. In the PLE spectrum of NIR luminescence, several PLE bands with sharp structures were observed at around 950, 750, 580, 420, 360 and 300 nm, which can be attributed to transitions from $^3A_{2g}$ ground state to $^3T_{2g}$, ^1E_g, $^3T_{1g}(^3F)$, ($^1A_{1g}$, $^1T_{2g}$), $^3T_{1g}(^3P)$ and (^1E_g, $^1T_{2g}$), respectively. The energy level calculation also confirms these assignments as shown in green lines (spin allowed transition) and gray lines (spin forbidden transition) in Figure 5. The PLE band at around 270 nm can be attributed to the charge transfer band from O^{2-} to Ni^{2+}.[45] The strongest PL line and PLE line are overlapped at 1012.5 nm (9877 cm^{-1}), which can be assigned to be the zero phonon line (ZPL) of the $^3T_{2g}$-$^3A_{2g}$ transition. Also, the PLE band at around 580 nm due to the $^3T_1(^3F) \leftarrow {}^3A_2$ has sharp lines (see Fig.S2 in Supporting Information). Consequently, the ZPL of $^3T_{1g}(^3F)$-$^3A_{2g}$ transition is

determined to be 626.6 nm (15960cm^{-1}). Different from the $^3T_{2g}$ ($t_{2g}^5e_g^3$) and $^3T_{1g}$ ($t_{2g}^5e_g^3$), the ^1E_g level has the same electronic configuration of $t_{2g}^6e_g^2$ as the ground state of $^3A_{2g}$ ($t_{2g}^6e_g^2$). In this case, the phonon sideband, PSB may not be observed because the vibrational interaction is weak due to the small configurational offset in a coordinate configuration diagram. Thus, the transition energy of ^1E_g-$^3A_{2g}$ is determined to be 749.5 nm (13340 cm^{-1}) based on the centroid energy. The obtained transition energies enable to estimate the Racah parameters (*B*, *C*) and crystal field parameter (*Dq*) by following Eqs. 1~3[44].

$$E\left(^3T_2\right) = 10Dq \quad \text{(Eq. 1)}$$

$$E\left(^3T_1(^3\mathrm{F})\right) = 15Dq + 7.5B - 0.5\sqrt{100Dq^2 - 180DqB + 225B^2} \quad \text{(Eq. 2)}$$

$$E\left(^1E\right) = 10Dq + 2C + 8.5B - 0.5\sqrt{400Dq^2 + 40DqB + 49B^2} \quad \text{(Eq. 3)}$$

The calculated values of *Dq*, *B*, and *C* are 988, 846 and 3490 cm^{-1}, and then the crystal field of 10*Dq/B* is located at 11.7. Compared to the reported 10*Dq*/*B* in various host compounds[44], the $LaAlO_3$ has a large value. It was reported that the $MgAl_2O_4$ shows the larger 10*Dq*/*B* (11.9)[33]. However, they used the peak energies instead of the ZPL energies, which may give the overestimation of *Dq* parameter. In $MgAl_2O_4$: Ni^{2+}, the PLE peak due to the $^3T_{2g}$←$^3A_{2g}$ is located at 970 nm, but the longer wavelength edge extends to around 1200 nm. In addition, the PL peak due to $^3T_{2g}$→$^3A_{2g}$ is located at 1180 nm. Based on the comparison of $^3T_{2g}$←$^3A_2$ PLE band wavelengths in $LaAlO_3$ and $MgAl_2O_4$, it is concluded that the $LaAlO_3$ has the strongest crystal field for Ni^{2+} among the hosts ever reported.

In order to construct the configurational coordinate diagram, the effective phonon energy ($\hbar\omega$) and the Huang-Rhys parameter (*S*) were estimated. Since the PL peak energy (E_{PLpeak}) at 300 K

and the ZPL energy (E_{ZPL}) due to the $^3T_{2g} \rightarrow {}^3A_{2g}$ transition are 9346 cm^{-1} and 9877 cm^{-1}, respectively, the Stokes shift (*SS*) was estimated to be 1062 cm^{-1} by the following equation.

$$SS = E_{PLEpeak} - E_{PLpeak} = 2\left(E_{ZPL} - E_{PLpeak}\right) = 2S\hbar\omega \quad \text{(Eq. 4)}$$

Based on the phonon sidebands (PSBs) in the PL spectrum of $^3T_{2g} \rightarrow {}^3A_{2g}$, the average effective phonon energy was estimated to be 121 cm^{-1} (see Fig. S3 and Table S2 in Supporting Information). Also, the average effective phonon energy in the PSBs of the $^3T_{1g} \leftarrow {}^3A_{2g}$ PLE band was estimated to be 128 cm^{-1} (see Fig. S2 and Table S1 in Supporting Information), which is very similar to that of the $^3T_{1g}$-$^3A_{2g}$ transition. Consequently, the Hung-Rhys parameter was estimated to be 4.39 from Eq. 4. The constructed configuration coordinate diagram is shown in Figure 6. Here the configurational offset of the ^1E excited state is assumed to be zero because of the same electronic configuration ($t_{2g}^6 e_g^2$) as the $^3A_2$ ground state. Also, the splitting of $^3T_{2g}$ by the crystal field is ignored in this diagram.

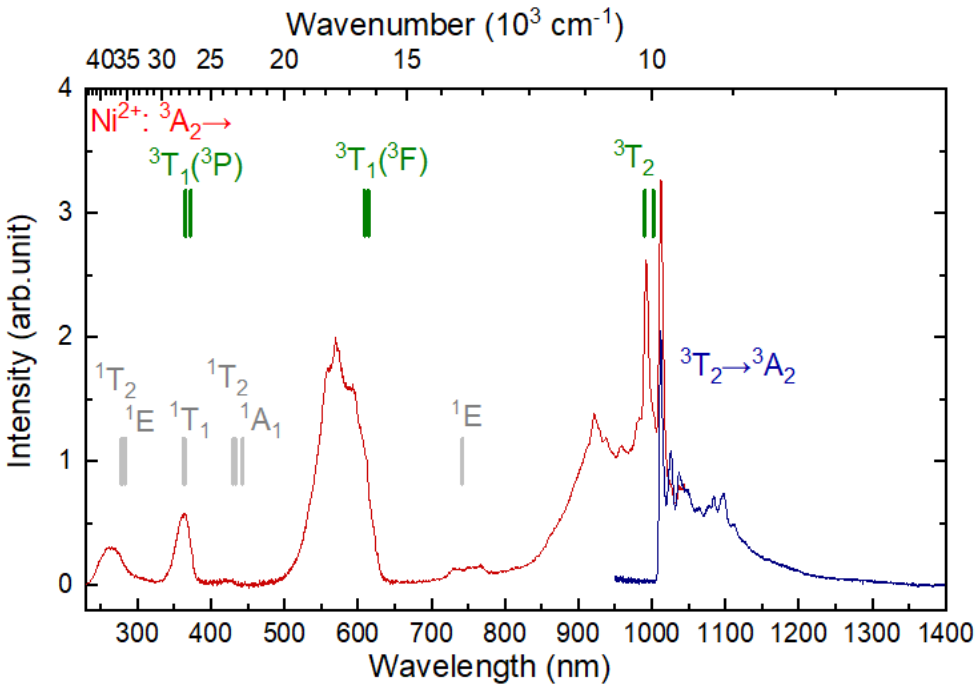

Figure 5. PL and PLE spectra of LAP:0.5%Ni-0.5%Sn at 3.6K with the calculated energy levels (gray lines and green lines).

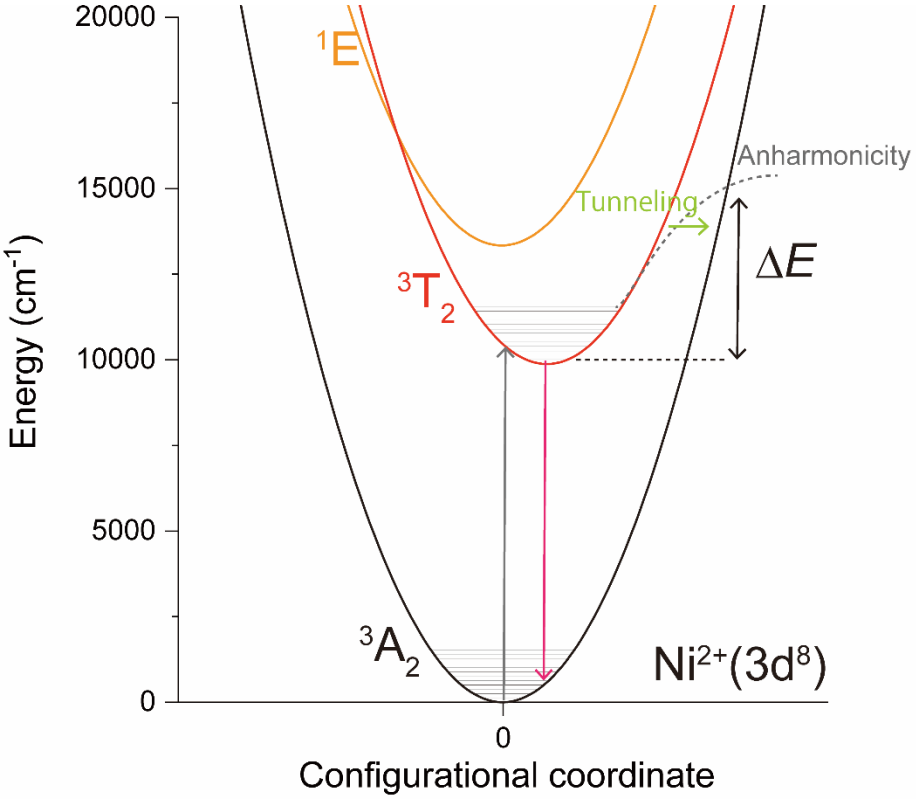

Figure 6. Configuration coordinate diagram of $LaAlO_3:Ni^{2+}$. The green arrow and the dotted curve express the schematic description of tunneling process and anharmonicity of vibrational potential, respectively.

Precisely, the Ni^{2+} ion experiences the S_6 symmetry in $LaAlO_3$. In this case, the $^3T_{2g}$ level in O_h symmetry is divided to $^3A_{1g}$ and ^3E_g levels by the crystal field theory. In the PL and PLE spectra of $^3T_{2g}$-$^3A_{2g}$ transition, several sharp lines beside the ZPL at 1012.5 nm (9877 cm^{-1}) originate from the PSBs. On the other hand, the strong PLE line at 992.5 nm (10076 cm^{-1}) does not seem to be a PSB because the corresponding PSB was not observed in the PL spectrum (see Fig. S3 and Table S2, S3 in Supporting Information). Also, the calculated $^3A_{1g}$ (9982 cm^{-1}) and ^3E_g

(10099 cm^{-1}) levels are similar to the observed two strong PLE lines. Thus, it is concluded that the observed sharp PLE lines at 1012.5 nm (9877 cm^{-1}) and 992.5 nm (10076 cm^{-1}) are attributed to the transition from $^3A_{2g}$ to $^3A_{1g}$ and ^3E_g, which are split from $^3T_{2g}$ by reducing symmetry.

Temperature-dependent spectroscopy

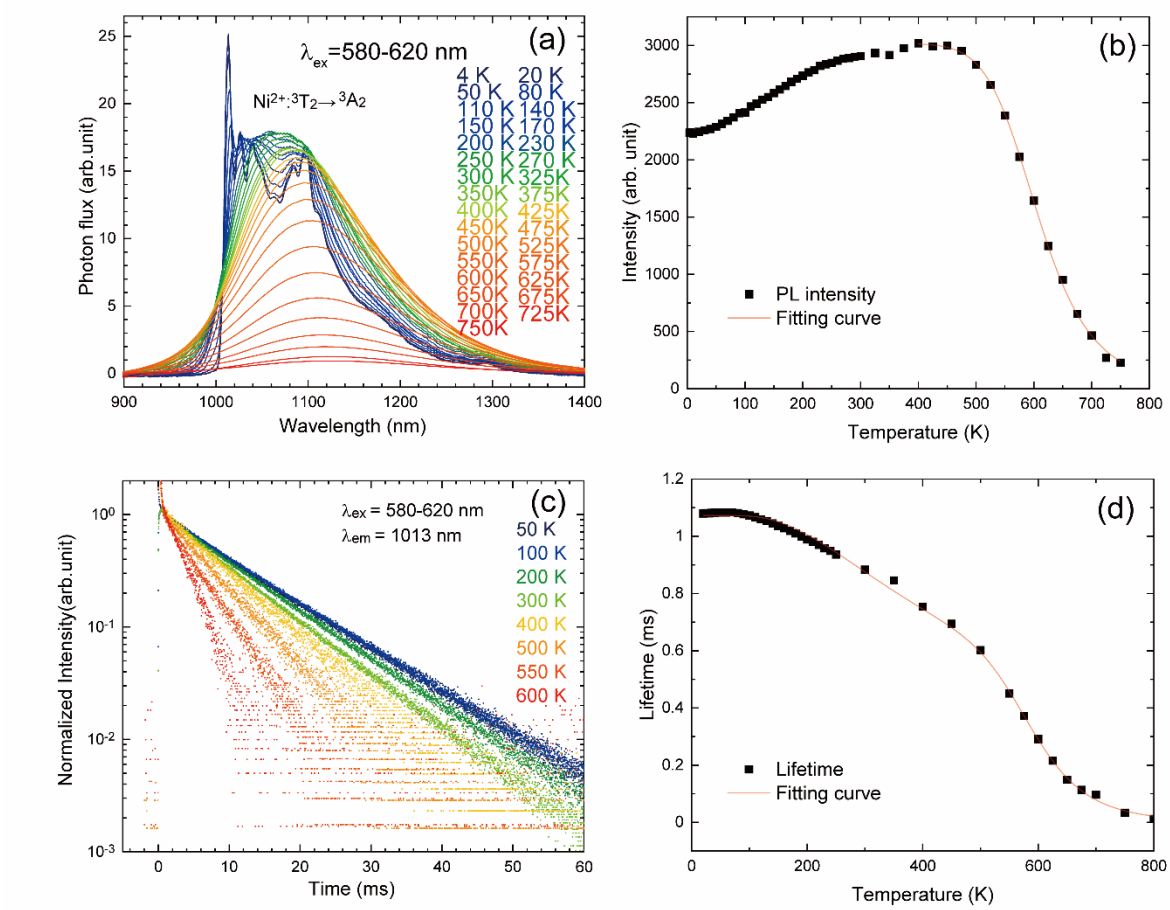

Figure 7. (a) NIR PL spectra at various temperatures (4 K-750 K), (b) temperature dependence of NIR PL integrated intensity, (c) NIR fluorescence decay curves at various temperatures (50K-

600K) and (d) Temperature dependence of fluorescent lifetime(Ni^{2+}:$^3T_2 \rightarrow {}^3A_2$) of the LAP:0.5%Ni-0.5%Sn sample.

Figure 7a shows the NIR PL spectra from 4 K to 750 K. The PL spectral structure of Ni^{2+}: $^3T_2 \rightarrow {}^3A_2$ is dramatically changed by temperature. The ZPL and PSBs broaden and become one broad luminescence band above around 250 K. The centroid wavelength is shifted to a longer wavelength with increasing temperature. At 300 K, the PL spectrum covers from around 950 nm to 1300 nm, and the centroid wavelength, peak wavelength and the FWHM (full width at half maximum) are 1100 nm, 1080 nm and 149 nm, respectively. These values are slightly different from that at ambient temperature. In addition, the thermal stability for NIR PL intensity is relatively high. Figure 7b shows the temperature dependence of the NIR PL integrated intensity. With increasing temperature, the intensity increases slightly up to 400 K and then decreases significantly. The quenching temperature ($T_{50\%}$), at which the intensity becomes half with respect to that at low temperature, is 608 K. Because of the increase of PL intensity in the range 4 K and 400 K, the quenching curve does not follow a simple single barrier quenching (Eq. 5) in the whole temperature range.

$$I_{(T)} = {I_0}\Big/{(1 + Cexp({-\Delta E}\Big/{_{kT}}))} \quad \text{(Eq.5)}$$

Here I_0 is the PL intensity at low temperature, C is the ratio of the attempt rate of the non-radiative process and the radiative decay rate, ΔE is the activation energy, k is Boltzmann constant and T is the temperature. By fitting the quenching curve above 400 K by the single barrier quenching (Figure 7b), the activation energy (ΔE) was estimated to be 0.68 eV.

In order to investigate the temperature-dependent luminescent properties in detail, fluorescent decay curves of Ni^{2+}:$^3T_2 \rightarrow {}^3A_2$ were measured at various temperatures (Figure 7c). In the semi-log plot of decay curves, the exponential profiles were observed within 100 ms at all temperatures. With increasing temperature, the fluorescent decay becomes shorter. The decay curves were fitted by the following equation $I = I_0 * \exp(-t/\tau)$ to estimate the lifetime. Figure 7d shows the temperature dependence of lifetime. The lifetime at 20 K is 1.08 ms, which is similar to $YAlO_3$:Ni^{2+} (1.02 ms) and $LaGaO_3$:Ni^{2+} (1.12 ms)[21]. With increasing temperature, the lifetime decreases slightly up to 500 K. The temperature dependence of lifetime in this temperature range is opposite to that of PL intensity. Thus, the decrease in the lifetime is caused by the increase in the radiative decay rate. This is because the population at higher energy levels interacting with phonons is increased by temperature and the radiative rate of PSBs is larger than that of ZPL. In other words, the anti-thermal quenching observed in the temperature dependence of integrated PL intensity (Figure 7b) is caused by the enhancement of total radiative rate due to the participation of the phonon induced transitions with the high radiative transition probability. The lifetime above 500 K decreases significantly, and this tendency is the same as the temperature-dependent PL intensity. This decrease of the lifetime is caused by the increase of the non-radiative decay rate. By taking into account the phonon-induced transition rate[46-48] and the nonradiative process, the temperature dependence of the lifetime was fitted by the following equation (Eq. 6).

$$\tau = \frac{1}{\Gamma_\nu \coth\left({}^{E_{pc}}/_{2kT}\right) + \Gamma_0 exp({}^{-\Delta E}/_{kT})} \quad \text{(Eq. 6)}$$

Γ_ν is the radiative rate, Γ_0 is the attempt rate of the non-radiative process and E_{pc} is the energy of phonon coupling to the $^3T_{2g}$-$^3A_{2g}$ transition. The obtained Γ_ν, Γ_0, E_{pc} and ΔE were estimated 9.3

$\times 10^2$ s^{-1}, 7.9×10^8 s^{-1}, 0.059 eV and 0.68 eV, respectively. The obtained activation energy of the quenching process from the lifetime is the same as that from the PL intensity. Here the quenching temperature ($T_{50\%}$) is the temperature to satisfy that the radiative rate and nonradiative rate become equal, $\Gamma_\nu \coth\left({}^{E_{pc}}/_{2kT}\right) = \Gamma_0 exp({}^{-\Delta E}/_{kT})$, and it was estimated to be 608 K. The quenching temperature estimated by the lifetime is also the same as that estimated by the PL intensity. The activation energy of 0.68 eV is smaller than the expected energy gap between the bottom of $^3T_{2g}$ potential curve and the cross point with $^3A_{2g}$ potential curve in the harmonic oscillation model (Figure 6). This can be related to several factors such as semi-quantitative estimation of energy gap based on the simple configurational coordinate diagram, tunneling process, anharmonicity of the vibrational potential and so on (Figure 6).

In order to compare the thermal stability for the luminescence intensity of $LaAlO_3:Ni^{2+}$, the quenching temperature of Ni^{2+}-doped phosphors are listed as shown in Table 1. The $T_{50\%}$ of $LaAlO_3:Ni^{2+}$ is the highest among the Ni^{2+}-doped phosphors ever reported. In order to investigate the quenching process, the luminescence peak wavenumber of Ni^{2+}: $^3T_2$-$^3A_2$ is collected (Table 1). If the quenching process is caused by thermally assisted crossover from the $^3T_2$ to $^3A_2$ level, the lower transition energy results in the smaller activation energy that causes severe quenching (Figure 6). Figure 8 shows the trend of $T_{50\%}$ of Ni^{2+}:$^3T_2$-$^3A_2$ luminescence as a function of luminescence peak wavenumber and the positive linear trend was observed. Therefore, the quenching process of Ni^{2+}:$^3T_2$-$^3A_2$ luminescence in almost all hosts including $LaAlO_3$ can be caused by the thermally assisted crossover. Because the $LaAlO_3:Ni^{2+}$ has the highest luminescence peak energy by the strong crystal field, the activation energy from $^3T_2$ to $^3A_2$ becomes large and the highest quenching temperature is realized.

Here, the difference of Ni^{2+}:$^3T_2 \rightarrow {}^3A_2$ PL peak wavenumber between $LaAlO_3$ and $YAlO_3$ is discussed. The lattice constant of $YAlO_3$ is smaller than that of $LaAlO_3$. In general, the small lattice constant leads the stronger crystal field. However, the crystal field of $YAlO_3$:Ni^{2+} is weaker than that of $LaAlO_3$:Ni^{2+} based on the Ni^{2+}:$^3T_2 \rightarrow {}^3A_2$ PL position (Table 1). The deviation from the general trend of the crystal field vs the lattice constant is also observed in Cr^{3+}-doped $LaAlO_3$ ($10Dq/B$=29.7)[49] and $YAlO_3$ ($10Dq/B$=26.5)[44]. These deviations can be caused by the distortion of the site for transition metal ion. The change of crystal field by distortion is well known in Ce^{3+}-doped garnets[50, 51].

Table 1. Quenching temperature ($T_{50\%}$) and peak wavenumber of Ni^{2+}:$^3T_2$-$^3A_2$ luminescence

Host	$T_{50\%}$	Luminescence peak wavenumber around 300 K	Reference
$LaAlO_3$	608 K	~9346 cm^{-1}	This work
$YAlO_3$	~490 K	~9130 cm^{-1}	[21]
$LaGaO_3$	~415 K	~8065 cm^{-1}	[21]
$LaMgAl_{11}O_{19}$	~315 K	(~8770 cm^{-1})*1	[20]
SrTiO3	~300 K	~8265 cm-1	[29]
CaTiO3	~300 K	~7576 cm-1	[29]
BaTiO3	~260 K	~6494 cm^{-1}	[29]
MgTiO3	~170 K	~5882 cm^{-1}	[29]
MgO	~520 K	~7500 cm^{-1}	[18]
$Y_3Al_2Ga_3O_{12}$	~515 K	~6897 cm^{-1}	[24]
MgF_2	~180 K	(~6100 cm^{-1}) *2	[25, 52]
$KZnF_3$	~205 K	(~5875 cm^{-1}) *3	[25]
$MgCl_2$	~220 K	~5300 cm^{-1}	[27]

$CsMgCl_3$	~190 K	~5200 cm^{-1}	[27]
$CsCdCl_3$	~18 0K	~4750 cm^{-1}	[27]
$CdCl_2$	~150 K	~4250 cm^{-1}	[27]

[*1]: Centroid energy at room temperature. [*2]: Peak energy at 195 K. [*3]: Centroid energy at 15 K.

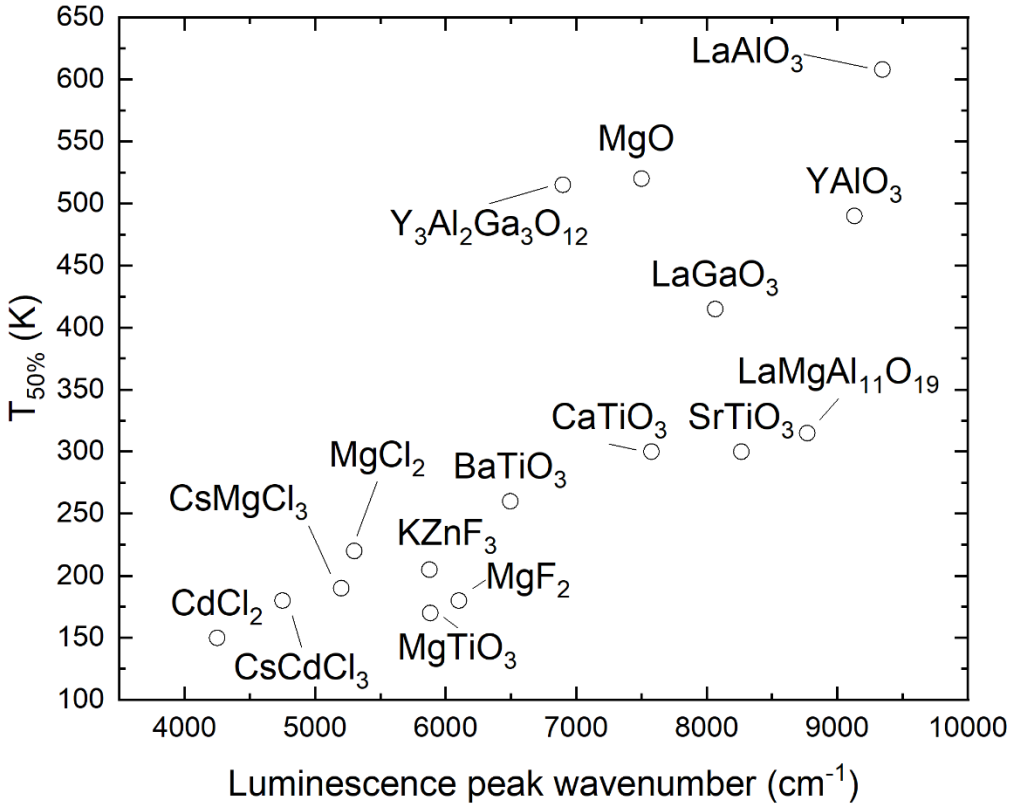

Figure 8. $T_{50\%}$ of Ni^{2+}:$^3T_2$-$^3A_2$ luminescence as a function of luminescence peak wavenumber.

Improvement of luminescence quantum efficiency

For the NIR LED applications, the luminescence quantum efficiency (QE) is very important. However, the QE of the NIR luminescence in the NIR-II region has been rarely reported due to

the limitation of the experimental setup. Here, the internal QE was investigated using the calibrated PL measurement system composed of an integrating sphere and an InGaAs PMT. It was discussed in Figure 3 that the luminescence intensity is increased by the Sn^{4+} charge compensator. Thus, the internal quantum efficiency of the $LaAlO_3$:0.5%Ni samples with different Sn^{4+} concentrations (0, 0.5, 1%) was measured by 590 nm excitation (Table 2). As expected in the PL spectra with Sn^{4+} charge compensator (Figure 3), the internal QE is improved from 0.005% to 3.0 % by codoping 0.5% Sn^{4+} charge compensator. The internal QE reaches 20.7 % by increasing to 1% Sn^{4+} concentration. On the other hand, the LAP:0.5%Ni^{2+}-2.5% Sn^{4+} shows weaker PL intensity compared with the 1% Sn^{4+} co-doped sample. The improvement of internal QE by the Sn^{4+} charge compensator up to 1% is due to the decrease of Ni^{3+}, which brings the quenching processes such as energy transfer, re-absorption and intervalence charge transfer. If we prepare the high-quality $LaAlO_3$ with only Ni^{2+} ions, the QE is expected to be more improved.

Table 2. Internal quantum efficiency of $LaAlO_3$:0.5%Ni-(0, 0.5, 1%)Sn^{4+}. Excitation wavelength is 590 nm and the integration area is 900 - 1600nm.

	0%Sn^{4+}	0.5%Sn^{4+}	1%Sn^{4+}
Internal QE	0.005	3.0 %	20.7%

Tuning luminescence wavelength

The advantage of the Ni^{2+}:$^3T_2$-$^3A_2$ transition is the tunability of luminescence wavelength by the crystal field. The composition of oxide perovskites can be changed widely, and the solid solutions can be prepared, resulting in the continuous tuning of luminescence wavelength. Figure **9** shows the normalized PL spectra of $LaAl_{1-x}Ga_xO_3$ solid solutions doped with 0.5%Ni-0.5%Sn by 600 nm excitation at ambient temperature. The PL peak wavelength shifts to a longer wavelength with increasing Ga content. The peak wavelengths of $LaAl_{1-x}Ga_xO_3$:Ni^{2+} with x= 0, 0.25, 0.5, 0.75, 1 are determined to be 1070, 1108, 1150, 1190, and 1235 nm, respectively. This result shows that the peak wavelength can be controlled between 1070 nm and 1235 nm by tuning the Ga content in the $LaAl_{1-x}Ga_xO_3$ host. The crystal structure of $LaAl_{1-x}Ga_xO_3$ belongs to the $R\bar{3}c$ (No. 167) trigonal space group except $LaGaO_3$ (*Pbnm*, No. 62, orthorhombic)[53], meaning that the longer wavelength shift up to x=0.75 is not related to the phase transition. The lattice constant of $LaAl_{1-x}Ga_xO_{12}$ ($x \leqq 0.9$) increases monotonically with increasing Ga content[53] because the ionic radius of Ga (0.62 Å in 6-fold coordination) is larger than that of Al (0.535 Å in 6-fold coordination)[54]. Because the size of the BO_6 octahedron in ABO_3 perovskites expands with increasing Ga content, the crystal field for Ni^{2+} in the octahedral site becomes weaker. In exchange for the longer wavelength shift by increasing Ga content, the quenching temperature is expected to be lower as shown in Figure 8. In actuality, the PL intensity shows decreasing tendency with increasing Ga content (see Fig. S4 in supporting information.). The internal QE of $LaAl_{1-x}Ga_xO_3$:0.5%Ni^{2+}-0.5%Sn^{4+} with x=0.25, 0.5, 0.75, 1 are 4.0, 0.7, 1.0, 0.1 %, respectively. The decreasing tendency of the internal QE with increasing Ga concentration can be also affected by $Ni^{2+/3+}$ ratio as shown in the Sn^{4+} concentration dependence of the internal QE in the LAP:Ni^{2+} samples (Table 2). In order to realize the longer wavelength NIR luminescence with high thermal stability in Ni^{2+}-doped NIR phosphors, it is necessary to find a strategy to minimize

the configurational offset and increase the curvature of potential curves in the configurational coordinate diagram in addition to the crystal field theory.

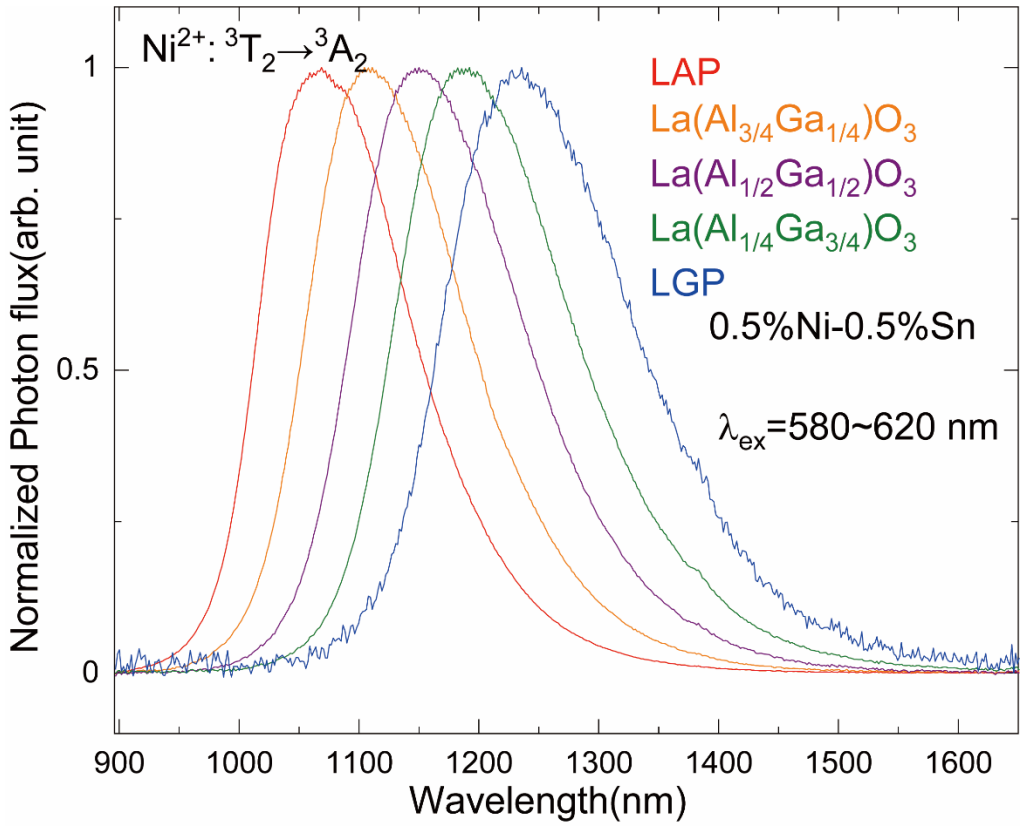

Figure 9. Normalized PL spectra of 0.5%Ni-0.5%Sn codoped solid solutions between $LaAlO_3$ (LAP) and $LaGaO_3$ (LGP).

Application as NIR broadband light source

The developed $LaAlO_3$:0.5%Ni-0.5%Sn phosphors can be used as suitable NIR light sources. As a proof of concept, transmittance spectra of organic substances (isopropyl alcohol, ethanol, Toluene, Acetone) was tested using NIR light, which is generated by the 600 nm excitation light and the $LaAlO_3$:0.5%Ni-0.5%Sn phosphor (Figure 10). In the transmittance spectra, several absorption peaks were observed at around 8500 cm^{-1}. These absorption peaks are attributed to

the second overtone of C-H bond stretching[55]. Also, the second overtones of N-H bond stretching and O-H bond stretching are located in the range between 10500 cm^{-1} and 9100 cm^{-1} [55]. Thus, the NIR light source using the $LaAlO_3$:0.5%Ni-0.5%Sn phosphor is suitable for sensing various organic substances.

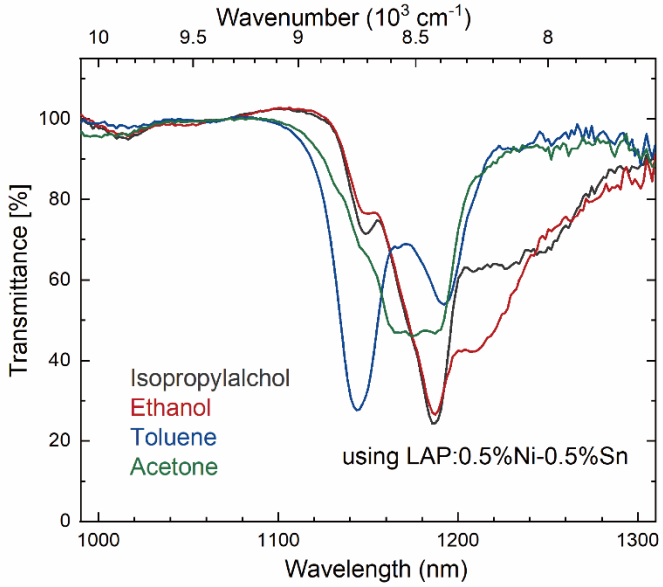

Figure 10. Transmittance spectra of organic substances (isopropyl alcohol, ethanol, toluene, acetone) using NIR broad light source using $LaAlO_3$:0.5%Ni-0.5%Sn phosphors.

Conclusions

The series of lanthanum-based perovskite NIR phosphors doped with Ni^{2+} have been prepared. The Ni^{2+}-doped $LaAlO_3$ shows the broad NIR luminescence peaking at 1067 nm due to the $^3T_2 \rightarrow {}^3A_2$ transition. The PL intensity is improved dramatically by co-doping with M^{4+} charge compensator (M =Sn, Hf, Ti, Zr). Among those samples, the Sn-codoped one shows the highest

PL intensity. Based on the XANES analysis, the valence state of Ni ion is changed by co-doping with Sn^{4+} from Ni^{3+} to Ni^{2+}. The detailed Ni^{2+} energy levels are determined by low-temperature spectroscopy. The ZPLs of $^3T_2$-$^3A_2$ and $^3T_1$-$^3A_2$ are determined to be 9877 cm^{-1} and 15960 cm^{-1}, respectively. The transition centroid energy of ^1E-$^3A_2$ is 13340cm^{-1}. Based on the obtained transition energies, the Racah parameters (*B*, *C*), crystal field parameter (*D*q) and crystal field (10*Dq*/*B*) were estimated to be 987.7 cm^{-1}, 845.9 cm^{-1}, 3491cm^{-1}, and 11.7, respectively. The estimated crystal field belongs to the highest class. The luminescence energy is the highest among the Ni^{2+}-doped NIR phosphors ever reported. It is also found that the $^3T_2$ excited level in the ideal O_h symmetry is split into two levels (^3E and $^3A_1$) due to the S_6 symmetry in the $LaAlO_3$ host based on the low-temperature spectroscopy. The temperature dependences of the $^3T_2$-$^3A_2$ NIR luminescence intensity and the lifetime enables us to estimate that quenching temperatures ($T_{50\%}$) are 608 K and 527 K, respectively. The $T_{50\%}$ of Ni^{2+}-doped $LaAlO_3$ is the highest value among the Ni^{2+}-doped NIR phosphors ever reported. Based on the positive linear trend in the plot of $T_{50\%}$ vs luminescence transition energy, the quenching process of almost all Ni^{2+} NIR phosphors including $LaAlO_3$:Ni^{2+} is concluded to be the thermally assisted crossover. The internal quantum efficiency of $LaAlO_3$:0.5%Ni^{2+}-1%Sn^{4+} was found to be 20.7 %. By preparing the solid solutions of $LaAl_{1-x}Ga_xO_3$:Ni^{2+}-Sn^{4+}, the NIR luminescence wavelength is successfully shifted like 1070 nm (x=0), 1108 nm (x=0.25), 1150 nm (x=0.50), 1190 nm (x=0.75), 1235 nm (x=1.0).

ASSOCIATED CONTENT

Supporting Information. The following files are available free of charge.

PL and PLE spectra with high wavelength resolution, peak energies of PSBs, and comparison of PL intensity in solid solutions between $LaAlO_3$ and $LaGaO_3$. (PDF)

AUTHOR INFORMATION

Corresponding Author

*E-mail: ueda-j@jaist.ac.jp

Author Contributions

JU and JX conceived the idea of the study. TM and S. Tanaka prepared the materials and investigated the optical properties. TN and TT measured and analyzed the NIR quantum efficiency. TM and JU drafted the original manuscript. S. Tanabe and JU supervised the conduct of this study. All authors reviewed the manuscript draft and revised it critically on intellectual content. All authors approved the final version of the manuscript to be published.

Funding Sources

JSPS KAKENHI (20H02438)

ACKNOWLEDGMENT

This research was financially supported by JSPS KAKENHI (grant number is 20H02438). The XANES measurements have been performed under the approval of the Photon Factory Program Advisory Committee (No. 2020G105). This work was supported by NIMS Joint Research Hub Program. We acknowledge Prof. Mikhail Brik of the University of Tartu for the energy level calculation.

REFERENCES

(1) Pasquini, C. Near infrared spectroscopy: A mature analytical technique with new perspectives – A review. *Analytica Chimica Acta* **2018**, *1026*, 8-36.

(2) Manley, M. Near-infrared spectroscopy and hyperspectral imaging: non-destructive analysis of biological materials. *Chem. Soc. Rev.* **2014**, *43* (24), 8200-8214, 10.1039/C4CS00062E.

(3) Luypaert, J.; Massart, D. L.; Vander Heyden, Y. Near-infrared spectroscopy applications in pharmaceutical analysis. *Talanta* **2007**, *72* (3), 865-883.

(4) Porep, J. U.; Kammerer, D. R.; Carle, R. On-line application of near infrared (NIR) spectroscopy in food production. *Trends Food Sci. Technol.* **2015**, *46* (2, Part A), 211-230.

(5) Bellon-Maurel, V.; Fernandez-Ahumada, E.; Palagos, B.; Roger, J.-M.; McBratney, A. Critical review of chemometric indicators commonly used for assessing the quality of the prediction of soil attributes by NIR spectroscopy. *TrAC, Trends Anal. Chem.* **2010**, *29* (9), 1073-1081.

(6) Huang, W.-T.; Rajendran, V.; Chan, M.-H.; Hsiao, M.; Chang, H.; Liu, R.-S. Near-Infrared Windows I and II Phosphors for Theranostic Applications: Spectroscopy, Bioimaging, and Light-Emitting Diode Photobiomodulation. *Adv. Opt. Mater.* **2022**, 2202061.

(7) Rajendran, V.; Chang, H.; Liu, R.-S. (INVITED) Recent progress on broadband near-infrared phosphors-converted light emitting diodes for future miniature spectrometers. *Opt. Mater. :X* **2019**, *1*, 100011.

(8) De Guzman, G. N. A.; Fang, M.-H.; Liang, C.-H.; Bao, Z.; Hu, S.-F.; Liu, R.-S. [INVITED] Near-infrared phosphors and their full potential: A review on practical applications and future perspectives. *J. Lumin.* **2020**, *219*, 116944.

(9) De Guzman, G. N. A.; Hu, S. F.; Liu, R. S. Enticing applications of near-infrared phosphors: Review and future perspectives. *J. Chin. Chem. Soc.* **2021**, *68* (2), 206-215.

(10) Fang, M.-H.; Bao, Z.; Huang, W.-T.; Liu, R.-S. Evolutionary Generation of Phosphor Materials and Their Progress in Future Applications for Light-Emitting Diodes. *Chemical Reviews* **2022**, *122* (13), 11474-11513.

(11) Smith, A. M.; Mancini, M. C.; Nie, S. Second window for in vivo imaging. *Nat. Nanotech.* **2009**, *4* (11), 710-711.

(12) Sordillo, L.; Pu, Y.; Pratavieira, S.; Budansky, Y.; Alfano, R. Deep optical imaging of tissue using the second and third near-infrared spectral windows. *J. Biomed. Opt.* **2014**, *19* (5), 056004.

(13) Zhao, F.; Song, Z.; Liu, Q. Advances in Chromium-Activated Phosphors for Near-Infrared Light Sources. *Laser Photonics Rev.* **2022**, *16* (11), 2200380.

(14) Kalisky, Y. Cr^{4+}-doped crystals: their use as lasers and passive Q-switches. *Prog. Quantum. Electron.* **2004**, *28* (5), 249-303.

(15) Tanabe, Y.; Sugano, S. On the Absorption Spectra of Complex Ions. I. *J. Phys. Soc. Jpn.* **1954**, *9* (5), 753.

(16) Tanabe, Y.; Sugano, S. On the Absorption Spectra of Complex Ions II. *J. Phys. Soc. Jpn.* **1954**, *9* (5), 766.

(17) Ralph, J. E.; Townsend, M. G. Fluorescence and absorption spectra of Ni2+in MgO. *J. Phys. C: Solid State Phys.* **1970**, *3* (1), 8-18.

(18) Iverson, M. V.; Windscheif, J. C.; Sibley, W. A. Optical parameters for the MgO:Ni2+ laser system. *Appl. Phys. Lett.* **1980**, *36* (3), 183-184.

(19) Donegan, J. F.; Bergin, F. J.; Glynn, T. J.; Imbusch, G. F.; Remeika, J. P. The optical spectroscopy of LiGa5O8: Ni2+. *J. Lumin.* **1986**, *35* (1), 57-63.

(20) Moncorge, R.; Benyattou, T.; Vivien, D.; Lejus, A. M. Ni2+ doped LaMgAl11O19: A potential vibronic laser system near 1.1 μm. *J. Lumin.* **1986**, *35* (4), 199-206.

(21) Koetke, J.; Huber, G.; Petermann, K. Spectroscopy of Ni^{2+}-doped garnets and perovskites for solid state lasers. *J. Lumin.* **1991**, *48-49*, 564-568.

(22) Zannoni, E.; Cavalli, E.; Toncelli, A.; Tonelli, M.; Bettinelli, M. Optical spectroscopy of $Ca_3Sc_2Ge_3O_{12}$:Ni^{2+}. *J. Phys. Chem. Solids* **1999**, *60* (4), 449-455.

(23) Yuan, L.; Jin, Y.; Zhu, D.; Mou, Z.; Xie, G.; Hu, Y. Ni^{2+}-Doped Yttrium Aluminum Gallium Garnet Phosphors: Bandgap Engineering for Broad-Band Wavelength-Tunable

Shortwave-Infrared Long-Persistent Luminescence and Photochromism. *ACS Sustain. Chem. Eng.* **2020**, *8* (16), 6543-6550.

(24) Yuan, L.; Jin, Y.; Wu, H.; Deng, K.; Qu, B.; Chen, L.; Hu, Y.; Liu, R.-S. Ni^{2+}-Doped Garnet Solid-Solution Phosphor-Converted Broadband Shortwave Infrared Light-Emitting Diodes toward Spectroscopy Application. *ACS Appl. Mater. Interfaces* **2022**, *14* (3), 4265-4275.

(25) Iverson, M. V.; Sibley, W. A. Temperature dependence of Ni2+ luminescence in KZnF3, MgF2 and MgO. *J. Lumin.* **1979**, *20* (3), 311-324.

(26) Stanley May, P.; Güdel, H. U. A previously unobserved luminescence of Ni^{2+} in Ni^{2+} : $KMgF_3$ and Ni^{2+} : $KZnF_3$. *Chem. Phys. Lett.* **1990**, *175* (5), 488-492.

(27) Stanley May, P.; Güdel, H. U. Infrared luminescence properties of Ni^{2+} in various chloride lattices: $CsCdCl_3$, $CsMgCl_3$, $CdCl_2$, and $MgCl_2$. *J. Lumin.* **1990**, *46* (5), 277-290.

(28) Luitel, H. N.; Mizuno, S.; Tani, T.; Takeda, Y. Effect of A-site cations on the broadband-sensitive upconversion of $AZrO_3:Er^{3+},Ni^{2+}$ (A = Ca, Sr, Ba) phosphors. *Opt. Mater.* **2017**, *64*, 314-322.

(29) Matuszewska, C.; Marciniak, L. The influence of host material on NIR II and NIR III emitting Ni^{2+}-based luminescent thermometers in $ATiO_3$: Ni^{2+} (A = Sr, Ca, Mg, Ba) nanocrystals. *J. Lumin.* **2020**, *223*, 117221.

(30) Martins, E.; Vieira, N. D.; Baldochi, S. L.; Morato, S. P.; Gesland, J. Y. Optical spectroscopy properties of $BaLiF_3$ doped with Ni^{2+}. *J. Lumin.* **1994**, *62* (6), 281-289.

(31) Martins, E.; Baldochi, S. L.; Morato, S. P.; Vieira, N. D.; Luci, A.; Casalboni, M.; Grassano, U. M.; Baldacchini, G.; Cremona; M.; et al. Fine structure of the absorption and

emission spectra of NI^{2+}-ions in $BALiF_3$. *Radiation Effects and Defects in Solids* **1995**, *135* (1-4), 15-18.

(32) Wyon, C.; Aubert, J. J.; Auzel, F. Czochralski growth and optical properties of magnesium-aluminium spinel doped with nickel. *J. Cryst. Growth* **1986**, *79* (1, Part 2), 710-713.

(33) Kuleshov, N. V.; Shcherbitsky, V. G.; Mikhailov, V. P.; Kück, S.; Koetke, J.; Petermann, K.; Huber, G. Spectroscopy and excited-state absorption of Ni^{2+}-doped $MgAl_2O_4$. *J. Lumin.* **1997**, *71* (4), 265-268.

(34) Brik, M. G.; Avram, N. M.; Avram, C. N.; Rudowicz, C.; Yeung, Y. Y.; Gnutek, P. Ground and excited state absorption of Ni^{2+} ions in $MgAl_2O_4$: Crystal field analysis. *J. Alloys Compd.* **2007**, *432* (1), 61-68.

(35) Jouini, A.; Yoshikawa, A.; Guyot, Y.; Brenier, A.; Fukuda, T.; Boulon, G. Potential candidate for new tunable solid-state laser between 1 and 2μm: Ni^{2+}-doped $MgAl_2O_4$ spinel grown by the micro-pulling-down method. *Opt. Mater.* **2007**, *30* (1), 47-49.

(36) Yu, G.; Wang, W.; Jiang, C. Linear tunable NIR emission via selective doping of Ni^{2+} ion into ZnX_2O_4 (X=Al, Ga, Cr) spinel matrix. *Ceram. Int.* **2021**, *47* (12), 17678-17683.

(37) Jin, M.; Li, F.; Xiahou, J.; Zhu, L.; Zhu, Q.; Li, J.-G. A new persistent luminescence phosphor of $ZnGa_2O_4$:Ni^{2+} for the second near-infrared transparency window. *J. Alloys Compd.* **2023**, *931*, 167491.

(38) Gao, Z.; Liu, Y.; Ren, J.; Fang, Z.; Lu, X.; Lewis, E.; Farrell, G.; Yang, J.; Wang, P. Selective doping of Ni^{2+} in highly transparent glass-ceramics containing nano-spinels $ZnGa_2O_4$ and $Zn_{1+x}Ga_{2-2x}Ge_xO_4$ for broadband near-infrared fiber amplifiers. *Sci. Rep.* **2017**, *7* (1), 1783.

(39) Walker, G.; Kamaluddin, B.; Glynn, T. J.; Sherlock, R. Luminescence of Ni^{2+} centers in forsterite (Mg_2SiO_4). *J. Lumin.* **1994**, *60-61*, 123-126.

(40) Zhou, S.; Feng, G.; Wu, B.; Jiang, N.; Xu, S.; Qiu, J. Intense Infrared Luminescence in Transparent Glass-Ceramics Containing β-Ga_2O_3:Ni^{2+} Nanocrystals. *The Journal of Physical Chemistry C* **2007**, *111* (20), 7335-7338.

(41) Wold, A.; Post, B.; Banks, E. Rare Earth Nickel Oxides. *Journal of the American Chemical Society* **1957**, *79* (18), 4911-4913.

(42) Koehler, W. C.; Wollan, E. O. Neutron-diffraction study of the magnetic properties of perovskite-like compounds $LaBO_3$. *J. Phys. Chem. Solids* **1957**, *2* (2), 100-106.

(43) Ravel, B.; Newville, M. ATHENA, ARTEMIS, HEPHAESTUS: data analysis for X-ray absorption spectroscopy using IFEFFIT. *J. Synchrotron Radiat.* **2005**, *12* (4), 537-541.

(44) Brik, M. G.; Camardello, S. J.; Srivastava, A. M.; Avram, N. M.; Suchocki, A. Spin-Forbidden Transitions in the Spectra of Transition Metal Ions and Nephelauxetic Effect. *ECS J. Solid. State Sci. Technol.* **2015**, *5* (1), R3067-R3077.

(45) Churmanov, V. N.; Sokolov, V. I.; Pustovarov, V. A.; Gruzdev, N. B.; Uimin, M. A.; Byzov, I. V.; Druzhinin, A. V.; Korolyov, A. V.; Kim, G. A.; Zatsepin, A. F.; et al. Charge transfer transitions in optical spectra of $Ni_cMg_{1-c}O$ oxides. *Low Temp. Phys.* **2017**, *43* (4), 520-525.

(46) Senden, T.; van Harten, E. J.; Meijerink, A. Synthesis and narrow red luminescence of Cs_2HfF_6:Mn^{4+}, a new phosphor for warm white LEDs. *J. Lumin.* **2018**, *194*, 131-138.

(47) Zhang, Z. Y.; Grattan, K. T. V. Temperature dependence of YAG:Cr^{3+} fluorescence lifetime up to 550 K. *J. Lumin.* **1994**, *62* (6), 263-269.

(48) Suchocki, A. B.; Gilliland, G. D.; Powell, R. C.; Bowen, J. M.; Walling, J. C. Spectroscopic properties of alexandrite crystals II. *J. Lumin.* **1987**, *37* (1), 29-37.

(49) Xu, J.; Murata, D.; So, B.; Asami, K.; Ueda, J.; Heo, J.; Tanabe, S. 1.2 μm persistent luminescence of Ho^{3+} in $LaAlO_3$ and $LaGaO_3$ perovskites. *Journal of Materials Chemistry C* **2018**, *6* (42), 11374-11383, 10.1039/C8TC04393K.

(50) Ueda, J.; Tanabe, S. Review of luminescent properties of Ce^{3+}-doped garnet phosphors: New insight into the effect of crystal and electronic structure. *Opt. Mater. :X* **2019**, *1*, 100018.

(51) Song, Z.; Liu, Q. Effects of Neighboring Polyhedron Competition on the 5d Level of Ce3+ in Lanthanide Garnets. *The Journal of Physical Chemistry C* **2019**, *123* (14), 8656-8662.

(52) Johnson, L. F.; Guggenheim, H. J.; Thomas, R. A. Phonon-Terminated Optical Masers. *Phys. Rev.* **1966**, *149* (1), 179-185.

(53) Matraszek, A.; Miller, M.; Singheiser, L.; Hilpert, K. Phase Composition and Vaporization Study of $LaGa_{1-x}Al_xO_3$, $0 \leq x \leq 1$, and $La_{0.9}Sr_{0.1}Ga_{0.8-x}Al_xMg_{0.2}O_{2.85}$, x= 0.1, 0.2, 0.3. *J. Am. Ceram. Soc.* **2003**, *86* (11), 1911-1917.

(54) Shannon, R. D.; Prewitt, C. T. Effective ionic radii in oxides and fluorides. *Acta Crystallographica, Section B: Structural Science, Crystal Engineering and Materials* **1969**, *25* (5), 925-946.

(55) Stuart, B. H. *Infrared spectroscopy: fundamentals and applications*; John Wiley & Sons, 2004.

Highly Thermal Stable Broadband Near-Infrared Luminescence in Ni^{2+}-doped $LaAlO_3$ with Charge Compensator